Electronic Supplementary Material (ESI) for Journal of Materials Chemistry A.
This journal is © The Royal Society of Chemistry 2019

Designing the Pd/O co-doped MoS_x for boosting hydrogen evolution reaction

Yingxin Zhan[+a], Xuemei Zhou[+a, b], Huagui Nie*[a], Xiangju Xu[a], Xiannuo Zheng[a], Junjie Hou[a], Huan Duan[c], Shaoming Huang*[b], Zhi Yang*[a]

Y. Zhan, X. Zhou, H. Nie, X. Xu, X. Zheng, J. Hou, Prof. Z. Yang

[a] Key Laboratory of Carbon Materials of Zhejiang Province, College of Chemistry and Materials Engineering, Wenzhou University, Wenzhou, 325035, PR China

Email: huaguinie@126.com ; yang201079@126.com;

X. Zhou, S. Huang

[b] School of Material and Energy, Guangdong University of Technology, Guangzhou, 510006, China

Email: smhuang@wzu.edu.cn

H. Duan

[c] School of Chemistry and Chemical Engineering, Southwest University, Chongqing, 400715, China

[+] These authors contributed equally to this work.

Experimental section

Electrode Preparation

Bare glassy carbon electrodes (GCE) (3 mm diameter, CH Instrument Inc.) were polished with different sizes alumina slurry on a microcloth and subsequently rinsed with ultrapure water and ethanol. The electrodes were then sonicated in ethanol, and dried under a gentle nitrogen stream. To prepare the working electrode, a 2 mg CNT sample (CNTs were purchased from Cnano Technology (Beijing) Limited (purity > 95%; diameter 11 nm; length = 10 μm (average); synthesis method, CVD)) was ultrasonically dispersed in the mixed solution of ethanol and H_2O (500 uL), and then 8μL of the resultant suspension was dropped onto the GCE surface and dried at room temperature. For comparison, a commercially available Pt/C-modified GCE (20 wt% Pt supported on carbon black, fuel cell grade from Alfa Aesar) was prepared in the same way.

Synthesis of Sub-MoS_x/CNTs

The hybrid catalysts were synthesized via a one-step electrochemical deposition method with a graphite rod using as the counter electrode and SCE (3 M KCl filled) as the reference electrode, wherein CNT-modified GCEs were soaked in a 2 mM $(NH_4)_2MoS_4$ aqueous solution containing 0.1 M $NaClO_4$, and the small size MoS_x was deposited in situ onto CNTs by a potential cycling experiment with the potential range from -0.1 to +1.0 V at a scan rate of 50 mV s^{-1}. After 30 electro-deposition cycles, the working electrode was rinsed with water gently and dried under vacuum at room temperature overnight.

Synthesis of i-t/MoS_x/CNTs

The hybrid catalysts were synthesized via electrochemical deposition method with a graphite rod using as the counter electrode and SCE (3 M KCl filled) as the reference electrode, wherein CNT-modified GCEs were soaked in a 2 mM $(NH_4)_2MoS_4$ aqueous solution containing 0.1M $NaClO_4$, and the MoS_x was deposited in situ onto CNTs by i-t experiment. The electrodeposition potential was -1.0 V vs. SCE. After 1800 s test, the working electrode was rinsed with water gently and dried at room temperature overnight.

Synthesis of Sub-MoS_x/CNTs/Pd_{gly}

The Sub-MoS_x/CNTs catalyst electrode was used as working electrode, a Pd wire as counter electrode, and a SCE (3 M KCl filled) electrode as reference in 0.5 M H_2SO_4 aqueous solutions containing Glycine (gly), which were purged with high purity nitrogen for at least 30 min prior to each measurement, and electrodeposited in the potential range from -0.2 to -0.7V for cyclic voltammograms (CV) at a scan rate of 100 mV/s. At the end of deposition, the working electrode was rinsed with water gently and dried at room temperature overnight. The parallel experiments using various deposition cycles were also carried out. For comparison, the Sub-MoS_x/CNTs-modified GCEs in H_2SO_4 solutions without gly were also treated under the same synthesis conditions (Sub-MoS_x/CNTs/Pd). In our work, The SCE reference electrode was calibrated with respect to reversible hydrogen electrode (RHE) by adding a value of (0.242 +0.0591pH) V before the measurements.

E (vs RHE) = E (vs SCE)+ E^0+ 0.0591pH. (E^0=0.242 V)

Synthesis of i-t/MoS_x/CNTs/Pd_{gly}

The i-t/MoS_x/CNTs catalyst electrode was used as working electrode, a Pd wire as counter electrode, and a SCE (3 M KCl filled) electrode as reference in 0.5 M H_2SO_4 aqueous solutions containing Glycine (gly), and electrodeposited in the potential range from -0.2 to -0.7 V for cyclic voltammograms (CV) at a scan rate of 100 mV/s. At the end of deposition, the working electrode was rinsed with water gently and dried at room temperature overnight. For comparison, the i-t/MoS_x/CNTs-modified GCEs in H_2SO_4 solutions without gly were also treated under the same synthesis conditions (i-t/MoS_x/CNTs/Pd).

Faradic efficiency

The Faradic efficiency is defined as the available efficiency of electrons involved in an electrochemical system. The Faradic efficiency can be calculated by the ratio of the practically producedH_2 content to its theoretical content. The former can be measured by gas chromatography. The theoretical H_2 evolution is calculated by the ratio of total buildup charge during electrolysis to the number of electrons required for H_2 evolution and Faraday's constant. The corresponding theoretically produced H_2 amount can be obtained according to this equation:[1]

$$n_{H_2} = Q/2F$$

Structure Characterization

X-ray photoelectron spectroscopy (XPS) measurements were carried out with an ultrahigh-vacuum setup, equipped with a monochromatic Al KR X-ray source and a highresolution Gammadata-Scienta SES 2002 analyzer. SEM images were obtained

with a JSM-6700 immersion scanning electron microscope. TEM analyses were carried out with a JEM-2100F instrument operating at 200 kV. Scanning transmission electron microscopy (STEM) characterizations were performed with an aberration-corrected Titan ChemiSTEM equipped with a probe corrector (CEOS). The Pd loading of samples were measured by VISTA-MPX ICP-OES.

Electrochemical Measurements

The electrochemical measurements were performed on a CHI 760D electrochemical workstation (Shanghai CHI Instruments Company) at 25ºC. A carbon catalyst electrode was used as working electrode, a graphite rod as the counter electrode, and a SCE (3 M KCl filled) electrode as reference. LSV measurements were performed in 0.5 M H_2SO_4 solutions (The 0.5 M H_2SO_4 solutions were saturated with N_2 prior to electrochemical measurements) at a scan rate of 5 mV s^{-1} to obtain the polarization curves. LSV curves were recorded by applying a potential sweep rate of 5 mV s^{-1} in the negative-going direction. The long-term stability were investigated by i-t tests at -0.2V (vs RHE, in 0.5 M H_2SO_4).To estimate the double-layer capacitance, cyclic voltammograms taken with various scan rates (20, 40, 80, 160, 200 mV s^{-1}) were used under the potential window of 0-0.3 V versus RHE. All data were reported without iR compensation. In all measurements, we used SCE as the reference electrode. It was calibrated with respect to RHE. The HER overpotentials, Tafel slopes and current densities in this paper and Tables and Figures have all been used absolute value.

Computational Details

All calculations were performed on the single MoS_2 layer in the framework of spin-

polarized DFT theory implemented in the all-electron code Fritz-Haber Institute ab initio molecules simulations package (FHI-aims). The exchange-correlation potentials were treated by the generalized gradient approximation (GGA) parameterized by Perdew, Burke, and Ernzerholf (PBE). The default 'tight' for H, O, S and 'light' for Mo, Pd element species were used in our work. To account for the weak non-covalent intermolecular interaction, these functionals were augmented by the van der Waals scheme of Tkatchenko and Scheffler. Defects were modelled in periodically repeated 7×7×1 supercells. Vacuum layers of 20 Å were introduced to minimize interactions between adjacent layers in all supercells. A (3×3×1) Monkhorst-Pack mesh of k-points was adopted to sample the Brillouin zone. Lattice geometries and atomic positions were fully relaxed until the charge density and the total energy were below of 10^{-4} eV·Å^{-3} and 10^{-5} eV, respectively.

Gibbs free energy of each HER step

To evaluate the relative stability of the doped MoS_2 monolayer, the formation energy (ΔE_{form}) was calculated as follows:

$$\Delta E_{form} = E_{tot}^{doped} - E_{tot}^{pure} - \sum_i n_i \mu_i \quad (1)$$

in which E_{tot}^{doped} and E_{tot}^{pure} were the total energy of the relaxed MoS_2 supercell with/without doped atoms, respectively. n_i was the number of doping element i being added/removed from the perfect supercell, and μ_i was the corresponding atomic chemical potential of each.

In acidic media, the HER process was mainly composed of H* intermediate formation and H_2 generation, which could be represented as

$$H^+ + e^- + MoS_2 \rightarrow H^*\text{-}MoS_2 \quad (2)$$

$$2H^*\text{-}MoS_2 \rightarrow H_2\uparrow + MoS_2 \quad (3)$$

The binding energy (ΔE_b) of hydrogen was defined as the energy difference between MoS_2 with H adsorbed (E_{MoS_2+H}) and the summation of the isolated H_2 molecules (E_{H_2}) and MoS_2 substrate (E_{MoS_2}):

$$\Delta E_b = E_{MoS_2+H} - E_{MoS_2} - 1/2E_{H_2} \quad (4)$$

where E_{MoS_2+H} was the total energy of the adsorbed system, E_{H_2} and E_{MoS_2} were the total energy of a isolate hydrogen molecule in the gas phase and the clean and dopant incorporated MoS_2 monolayer computed in a supercell.

The Gibbs free energy of HER intermediate was then calculated following the approach of Nørskov et al:

$$\Delta G = \Delta E_b + \Delta ZPE - T\Delta S \quad (5)$$

where, zero point energies (ΔZPE) and entropy changes (ΔS) were employing as implemented in prior works and tabulated values (webbook.nist.gov/chemistry/).

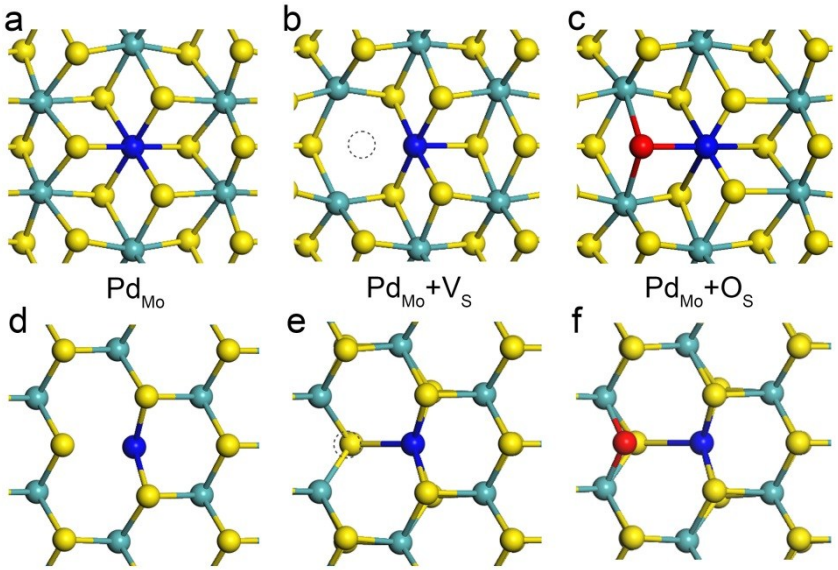

Fig. S1 Schematic illustration of the defecs in 1T-MoS_2 (a~c) and 2H-MoS_2 (d~f). The blue, olivine, yellow and red balls were Pd, Mo, S and O atoms, respectively.

Supplementary note:

For the Pd_{Mo} defect, Pd^{4+} ions were thermodynamically metastable when incorporated into the fully sulfurized monolayer under high sulfur pressuresor ultra-low temperatures. The DFT optimized structure of the 1T-Pd_{Mo}-MoS_2 demonstrated that Pd-incorporation was stabilized by six neighboring sulfur atoms that presented an octahedral coordination environment for the d^6 metal center. But the case of 2H-Pd_{Mo}-MoS_2 was more favorable to form, since the Pd_{Mo} defects in the 2H-MoS_2 caused a significant restructuring of the nearest S atoms and provided an approximate flattened square-planar sulfur coordination for the d^8 metal center. Therefore, the unsaturated S atoms surrounding the defects would become more active and cut down on the thermodynamic driven force to create the sulfur vacancies for non-metal (NM) atoms' location.

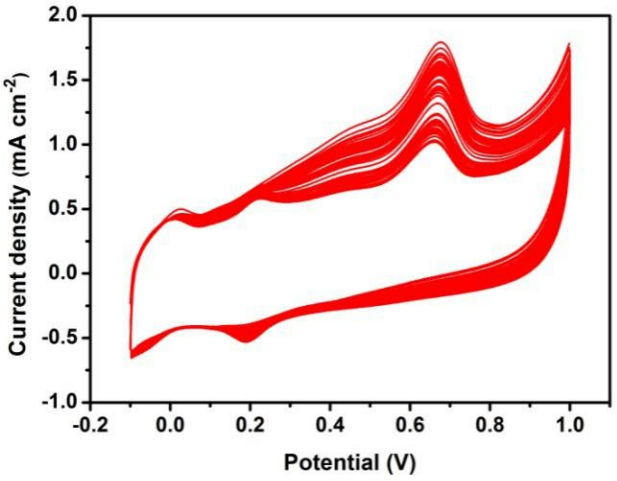

Fig. S2 The CVs recorded during the procedure.

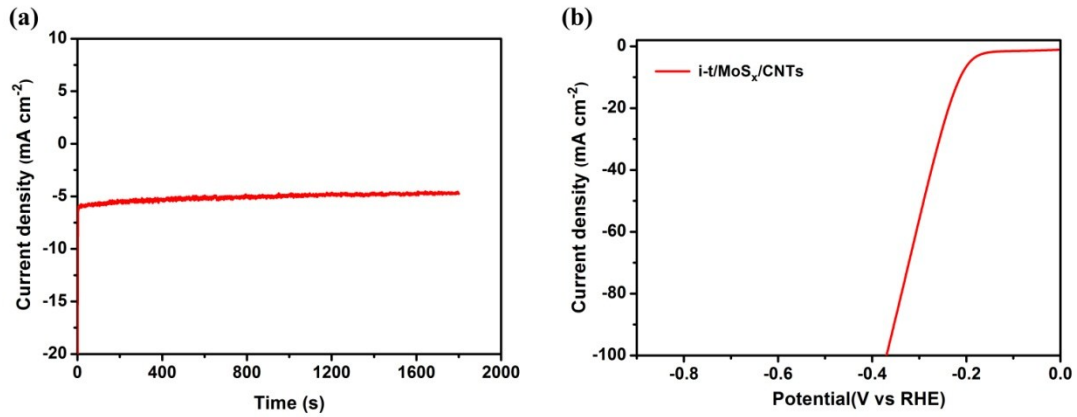

Fig. S3 (a) The i-t curve recorded during the procedure. (b) The polarization curves for i-t/MoS_x/CNTs in a 0.5 M H_2SO_4 solution at a scan rate of 5 mV s^{-1}.

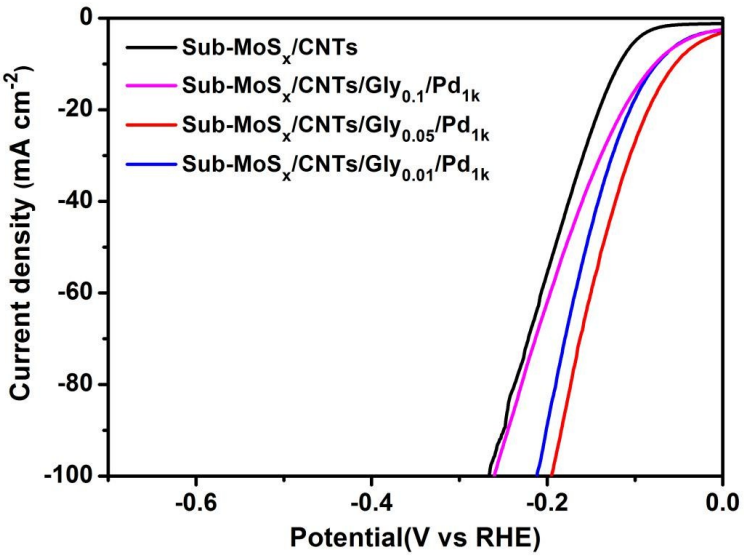

Fig. S4 The polarization curves for various gly concentrations of the catalysts.

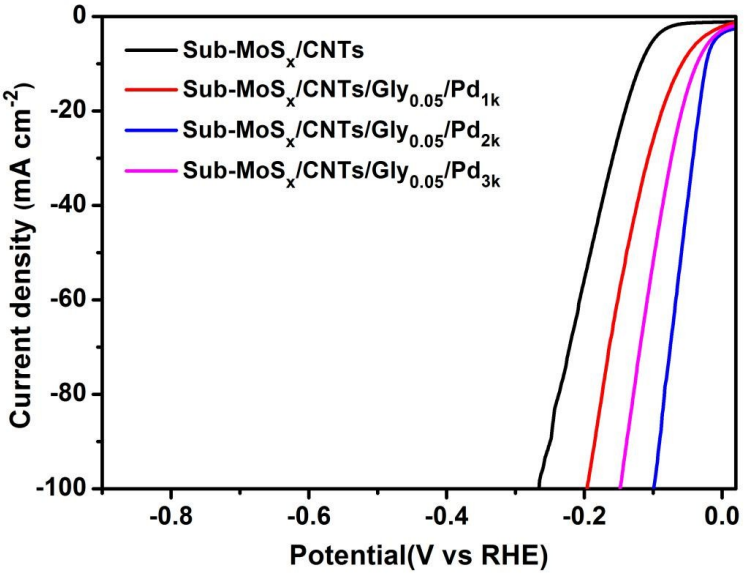

Fig. S5 The polarization curves for various potential cycles of the catalysts.

Table S1. The parallel experiments and the overpotential of different samples at various current density.

Catalyst	**glycine concentrations (mol/L)**	**deposition cycles (cycles)**	**η at corresponding j=10 $mAcm^{-2}$ (mV vs RHE)**	**η at corresponding j=100 $mAcm^{-2}$ (mV vs RHE)**
Sub-MoS_x/CNTs			118	266
i-t/MoSx/CNTs			209	370
Pt/C			34	153
pristine CNTs			645	/
Sub-MoS_x/CNTs/$Gly_{0.05}$/Pd_{1k}	0.05	1000	55	196
Sub-MoS_x/CNTs/$Gly_{0.01}$/Pd_{1k}	0.01	1000	76	212
Sub-MoS_x/CNTs/$Gly_{0.1}$/Pd_{1k}	0.1	1000	78	260
Sub-MoS_x/CNTs/$Gly_{0.05}$/Pd_{2k} (denoted Sub-MoS_x/CNTs/Pd_{gly})	**0.05**	**2000**	**23**	**100**
Sub-MoS_x/CNTs/$Gly_{0.05}$/Pd_{3k}	0.05	3000	37	148
Sub-MoS_x/CNTs/Pd_{2k} (denoted Sub-MoS_x/CNTs/Pd)		2000	36	162
i-t/MoS_x/CNTs/Pd_{gly}	0.05	2000	12	237
i-t/MoS_x/CNTs/Pd		2000	118	241

Supplementary note 1:

Fig. S4 and Table S1 demonstrate that Sub-MoS_x/CNTs/Pd_{gly} catalyst with glycine concentration of 0.05 M generated a higher catalytic current than that of samples with other glycine concentrations (0.01 and 0.1 M), hence the 0.05 M of glycine was considered as the suitable concentration for subsequent parallel experiment. Parallel experimental trials employing various numbers of potential cycles were performed (Fig. S5) and the HER performance results of as-grown samples were shown in Table S1. It was found that the Sub-MoS_x/CNTs/Pd_{gly} catalyst showed the highest catalytic current among all the catalysts, so this sample was chosen as the optimal host material for subsequent experiments.

The concentration of glycine could affect the rate of palladium ion deposition on the working electrode by complexation. When the concentration is low and the complexation is weak, the palladium ion is fast migration to the working electrode during the deposition process, which could easily form palladium dendrite. When the concentration is high and strong complexation, the migration rate of palladium ion is too slow, which resulted in the time-consuming reaction and too low loading on the surface of the working electrode.

The activity of the Sub-MoS_x/CNTs/Pd_{gly} increased with the number of potential cycles, however, the catalytic activities of the catalyst would decrease with the CVs scans over 3000 cycles, which could be attributed that high loading and aggregated palladium would decrease the interfacial area between the electrode and the electrolyte."

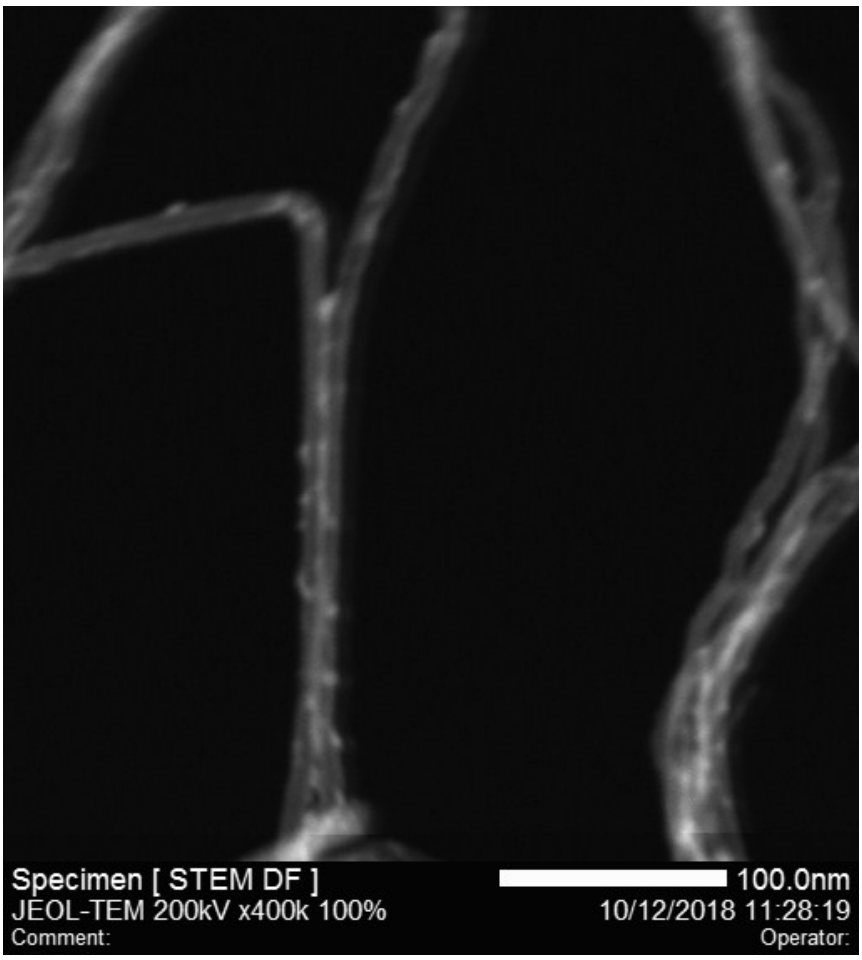

Fig. S6 STEM images of Sub-MoS_x/CNTs catalyst.

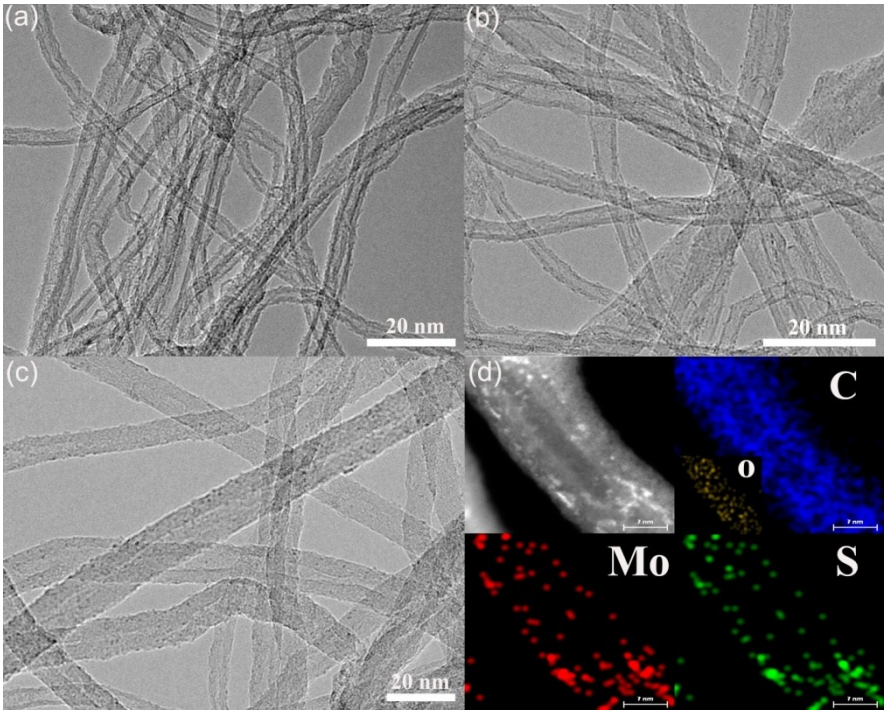

Fig. S7 Characterizations of the Sub-MoS_x/CNTs hybrid catalysts: (a) ,(b) ,(c)TEM image, (d) STEM and corresponding element maps (scale bar = 7 nm).

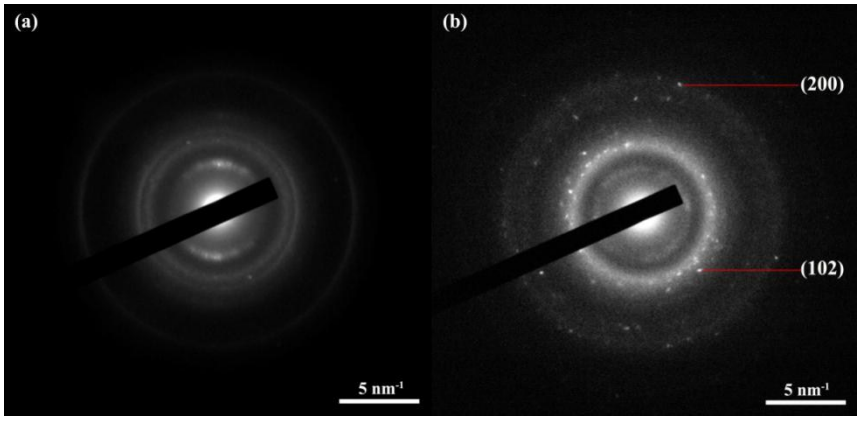

Fig. S8 The electron diffraction pattern of Sub-MoS_x/CNTs/Pd_{gly} and i-t/MoS_x/CNTs/Pd.

Supplementary note 2:

The final product component was characterized by the selected-area electron-diffraction (SAED), as given in Fig. S8. Fig. S8a contains blurry rings generated by the Sub-MoS_x/CNTs/Pd_{gly} that imply non perfect ordering of the catalyst, further confirming that the catalyst may display an amorphous structure. The SAED of i-t/MoS_x/CNTs/Pd exhibits several rings which could be attributed to Pd crystal grains (Fig. S8b). The component of as-grown products are also analyzed by XRD, however, no effective results have been obtained due to its amorphous structure and low loading amount.

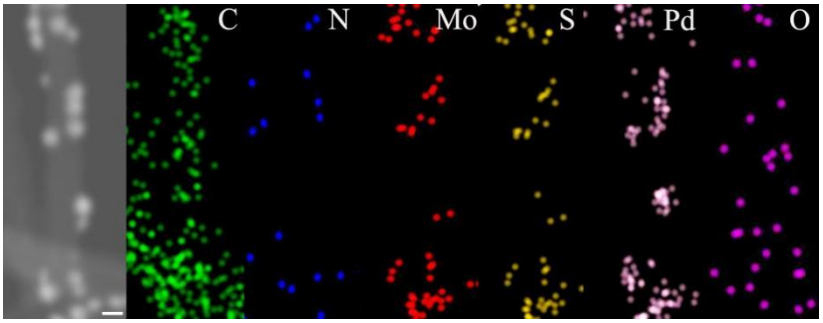

Fig. S9 The STEM and corresponding element maps (scale bar =70 nm) of Sub-MoS_x/CNTs/Pd_{gly}.

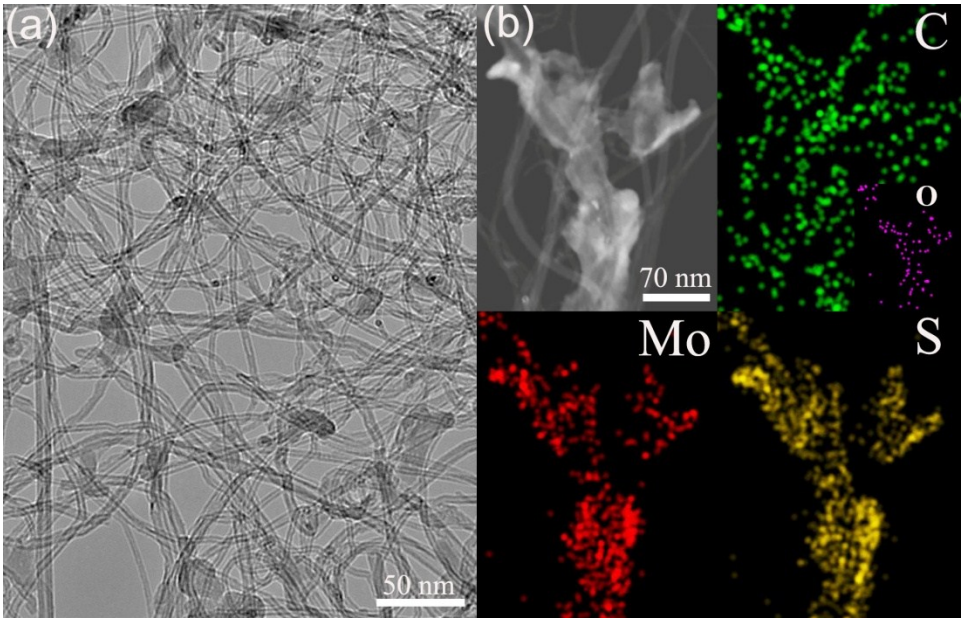

Fig. S10 Characterizations of the i-t/MoS_x/CNTs hybrid catalysts: (a) TEM image, (b) STEM and corresponding element maps.

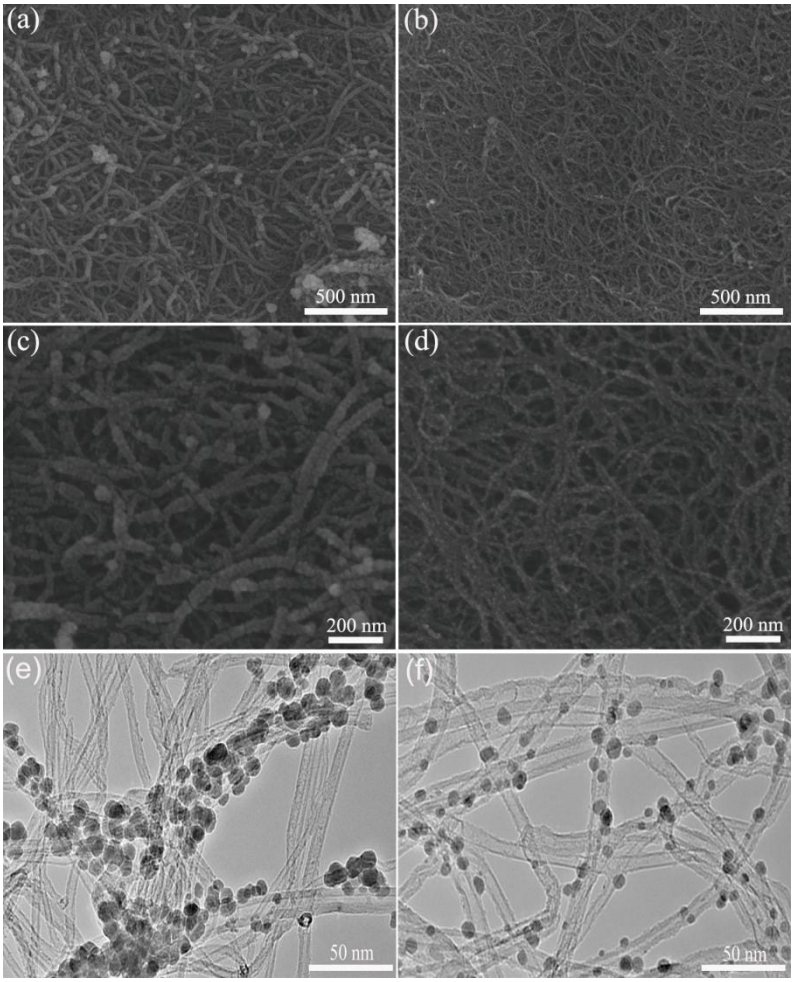

Fig. S11 Characterizations of the Sub-MoS_x/CNTs/Pd hybrid catalysts: (a),(c) SEM image, (e) TEM image. Characterizations of the Sub-MoS_x/CNTs/Pd_{gly} hybrid catalysts: (b),(d) SEM image, (f) TEM image.

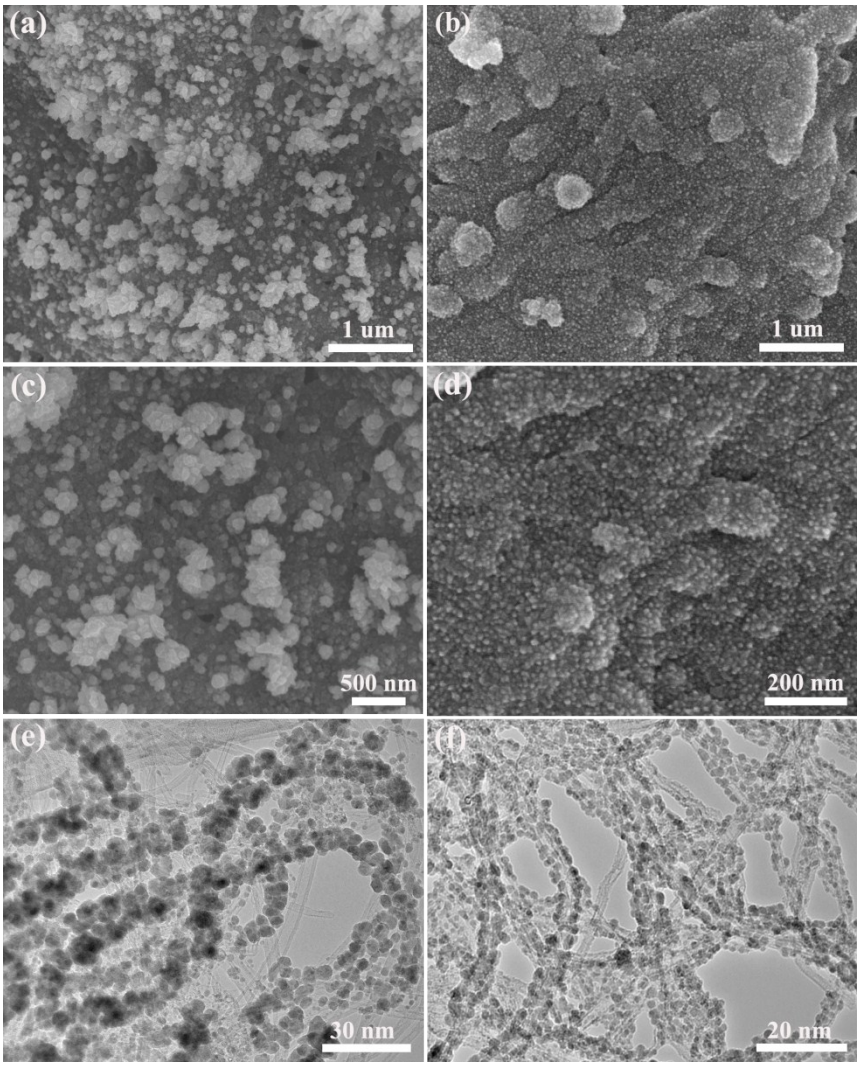

Fig. S12 Characterizations of the i-t/MoS_x/CNTs/Pd hybrid catalysts: (a),(c) SEM image, (e) TEM image. Characterizations of the i-t/MoS_x/CNTs/Pd_{gly} hybrid catalysts: (b),(d) SEM image, (f) TEM image.

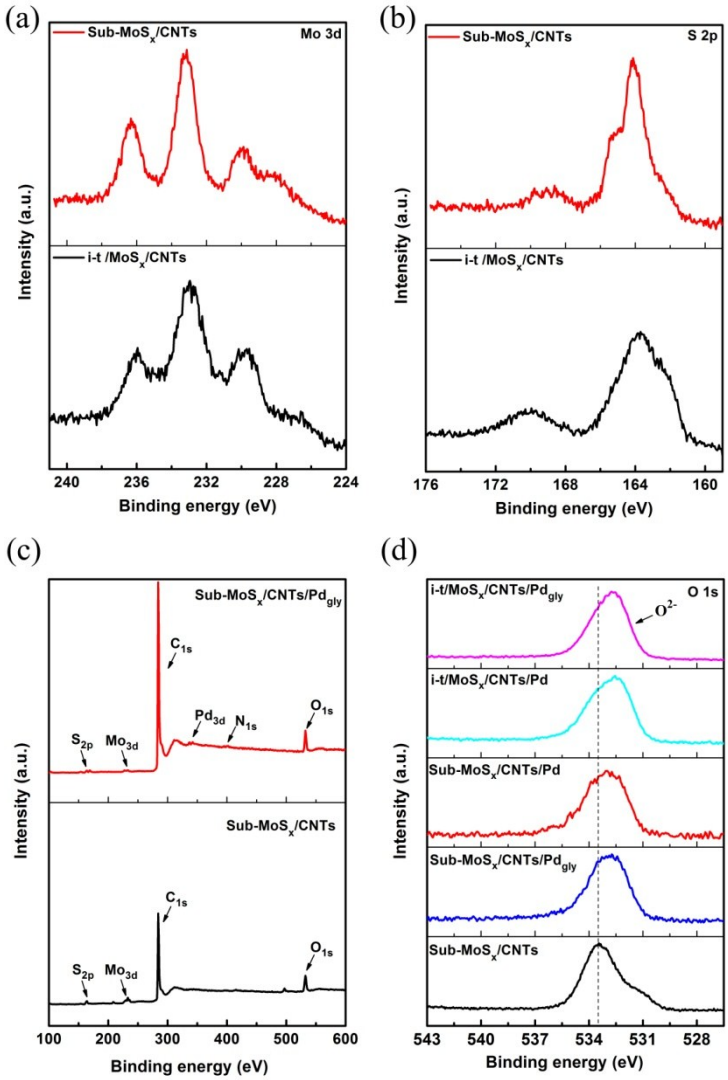

Fig. S13 The Mo 3d and S 2p spectrum of the Sub-MoS_x/CNTs and i-t/MoS_x/CNTs. (a) Mo 3d, (b) S 2p. (c) The XPS patterns of the Sub-MoS_x/CNTs/Pd_{gly}. (d) The O 1s spectrum of the Sub-MoS_x/CNTs and Sub-MoS_x/CNTs/Pd_{gly}.

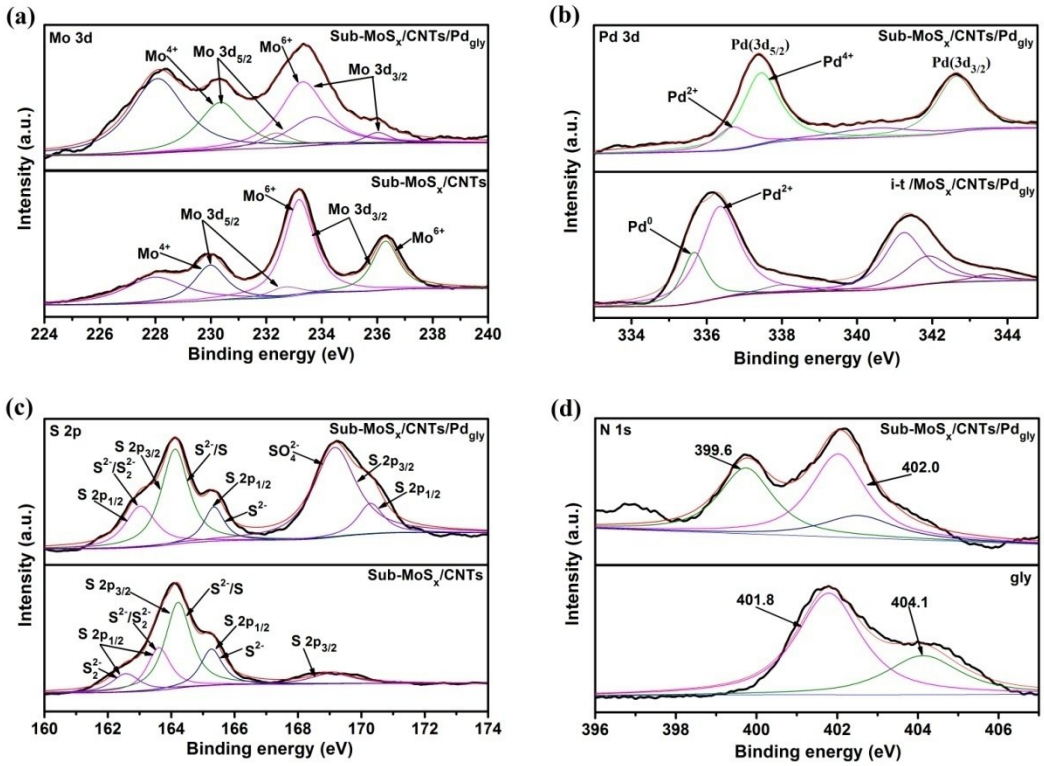

Fig. S14 Structural characterizations of the catalysts: (a) Mo 3d, (b) Pd 3d, (c) S 2p and (d) N 1s fitting spectra of the hybrid catalysts.

Supplementary note 3:

According to the fitting results, the both Mo (IV) and Mo (VI) could be observed (Fig. S14a). In Fig.S14a, the deconvolution of the Mo 3d region by peak fitting reveals that the binding energies of 229.9 eV is attributed to Mo (IV), and another two distinct characteristic peaks at 233.2 eV and 236.2 are due to the Mo(VI) ion. Fig. 3a shows the Mo 3d peaks of the samples prepared with the upgraded sacrificial-counter-electrode method all shift to lower binding energies (BEs), revealing that the Mo (VI) has been reduced to Mo (IV).[2,3] Fig. 3b shows the Pd 3d peaks and it can be seen that the binding energies of Pd $3d_{5/2}$ are 336.3 and 337.4 eV, which can be assigned to Pd (II) and Pd (IV), respectively. Fig. S14b shows that the Pd $3d_{5/2}$ peaks of Sub-MoS_x/CNTs/Pd_{gly} shift to higher BEs compared with those of the i-t-MoS_x/CNTs/Pd_{gly} samples, indicating that the valence state of Pd is Pd (IV) and Pd (II) in Sub-MoS_x/CNTs/Pd_{gly}, but Pd (II) and Pd (0) in the Pd dendrites in i-t-MoS_x/CNTs/Pd_{gly}, which is consistent with the previous reports.[4-6] The S 2p spectrum in Fig. S14c shows a broad and complex peak. The binding energies at 162.4 eV can be attributed to terminal S_2^{2-} ligands, and the binding energies at 163.6 eV represents bridging S_2^{2-} and/or apical S^{2-} ligands. The S $2p_{3/2}$ at higher energy (164.1 eV) can be attributed to residual sulfur from the electrodeposition reactant/or apical S^{2-} ligands, the binding energies at 165.2 eV may be attributed to apical S^{2-} ligands. It is apparent that the S 2p peaks were shifted to higher binding energies after the potential cycling process, which reveals that the S^{2-} ions are gradually transformed into SO_x^{2-}.[7,8] The peaks at 401.8 and 404.1 eV could be corresponding to C-N and N-H. Fig. S14d show a shift towards lower BEs compared with the original Gly sample, which may be attributed to the formation of complexes held together by Pd-N bonds (399.6 eV).[9]

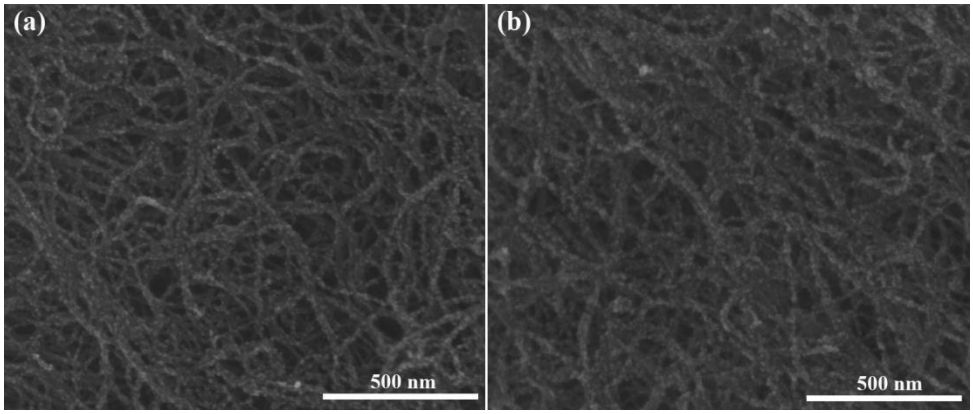

Fig. S15 SEM images the morphology of the catalysts before (a) and after stability test (b).

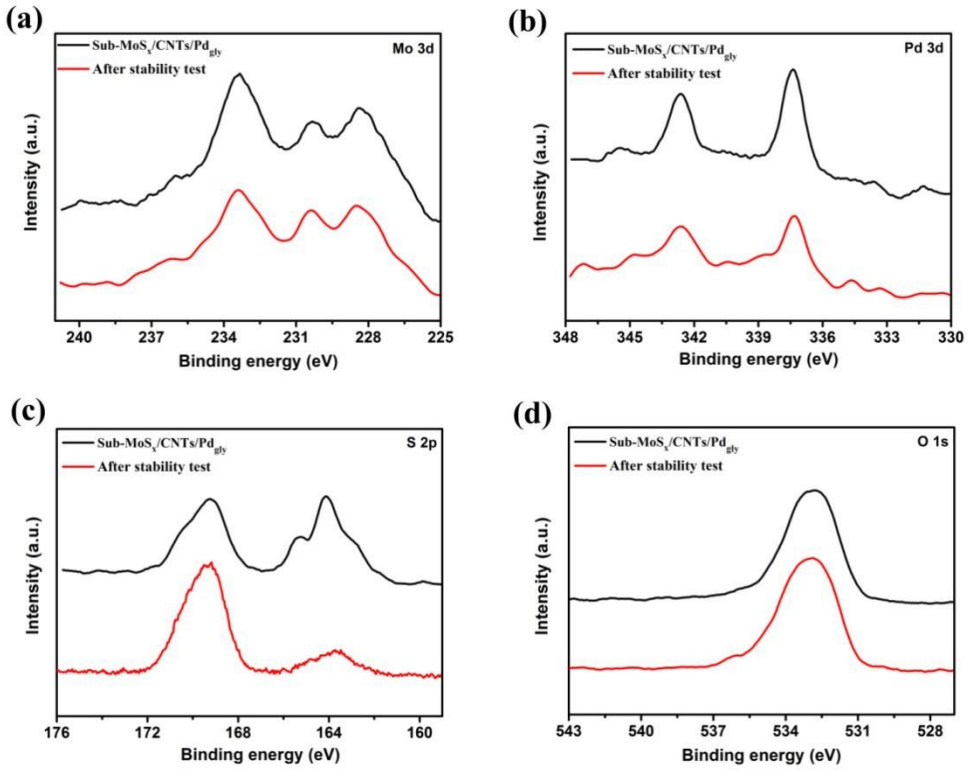

Fig. S16 Structural characterizations of the catalysts before and after stability test. (a) Mo 3d, (b) Pd 3d, (c) S 2p , (d) O 1s spectra of the catalysts.

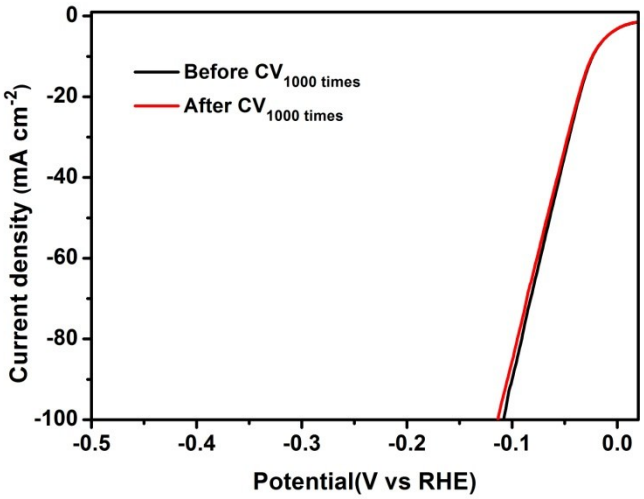

Fig. S17 The polarization curves recorded before and after the test.

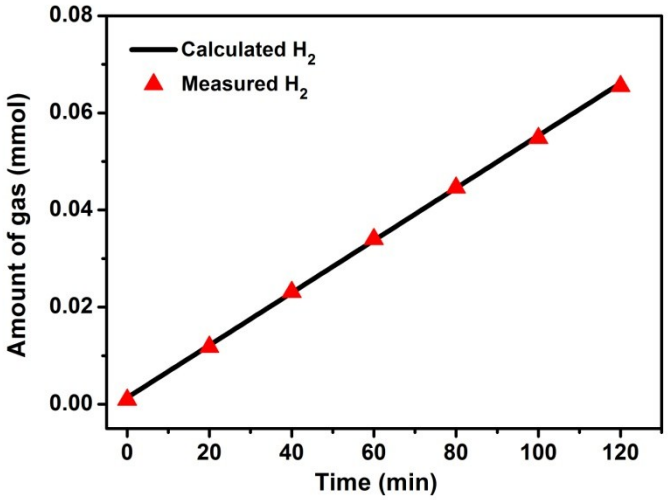

Fig. S18 The amount of hydrogen theoretically calculated and experimentally measured versus time for Sub-MoS_x/CNTs/Pd_{gly} in 0.5 M H_2SO_4.

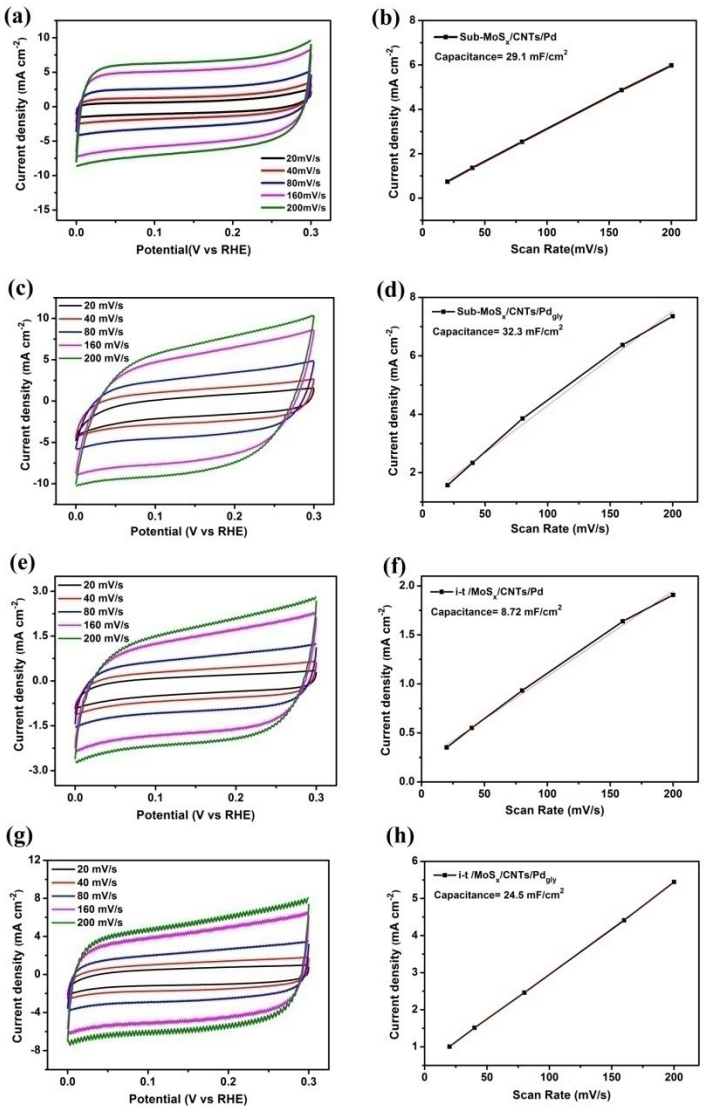

Fig. S19 The standard CV curves and C_{dl} of different samples with different scan rates.

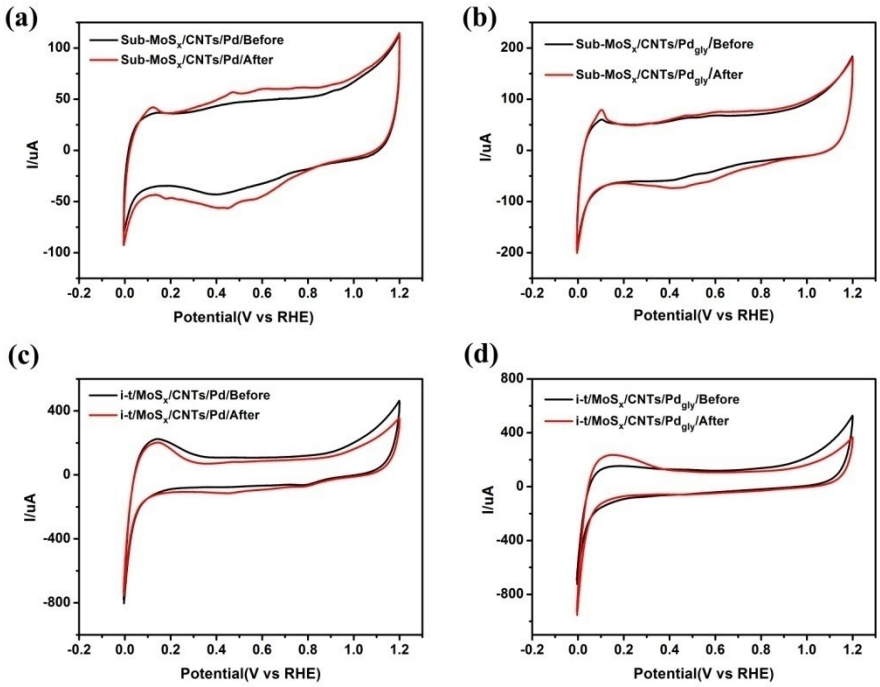

Fig. S20 The CVs recorded before and after the HER treatment of the Sub-MoS_x/CNTs/Pd_{gly}, Sub-MoS_x/CNTs/Pd, i-t/MoS_x/CNTs/Pd_{gly} and i-t/MoS_x/CNTs/Pd catalysts.

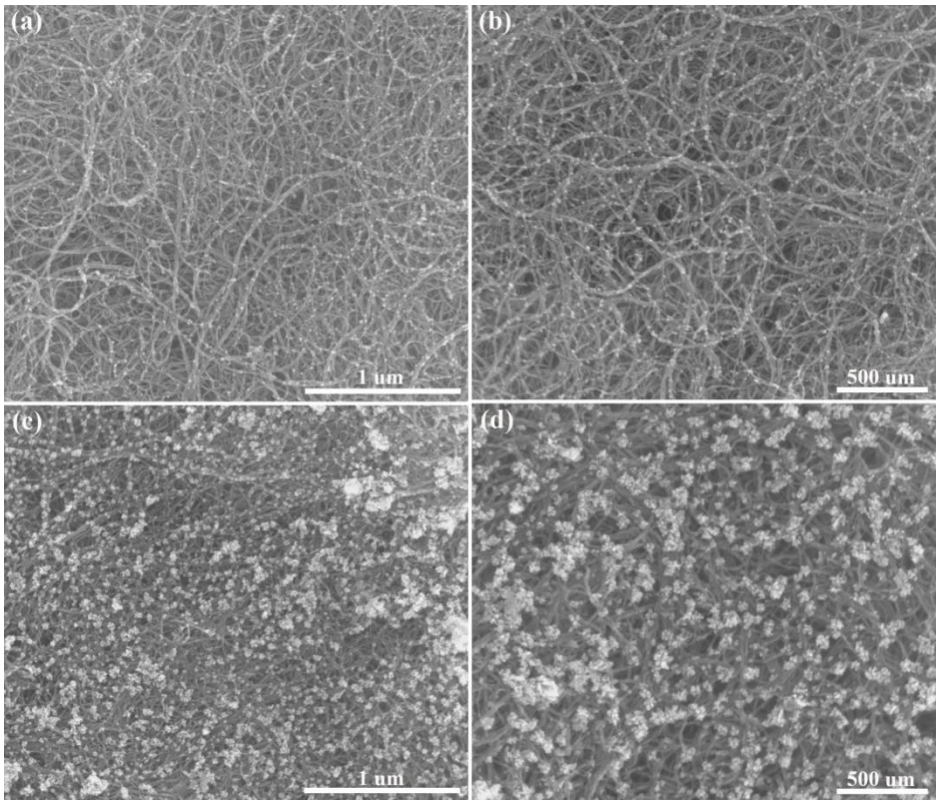

Fig. S21 Characterizations of the CNTs/Pd_{gly} hybrid catalysts: (a), (b) SEM images. Characterizations of the CNTs/Pd hybrid catalysts: (c), (d) SEM images.

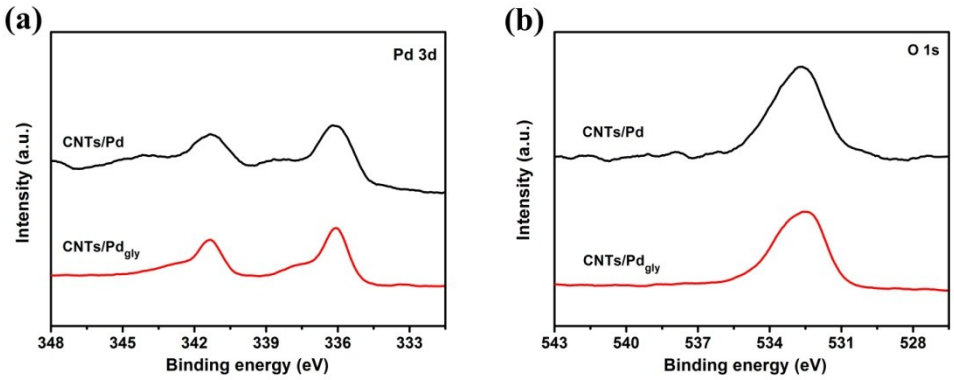

Fig. S22 Structural characterizations of the catalysts: (a) Pd 3d and (b) O 1s spectra of the hybrid catalysts.

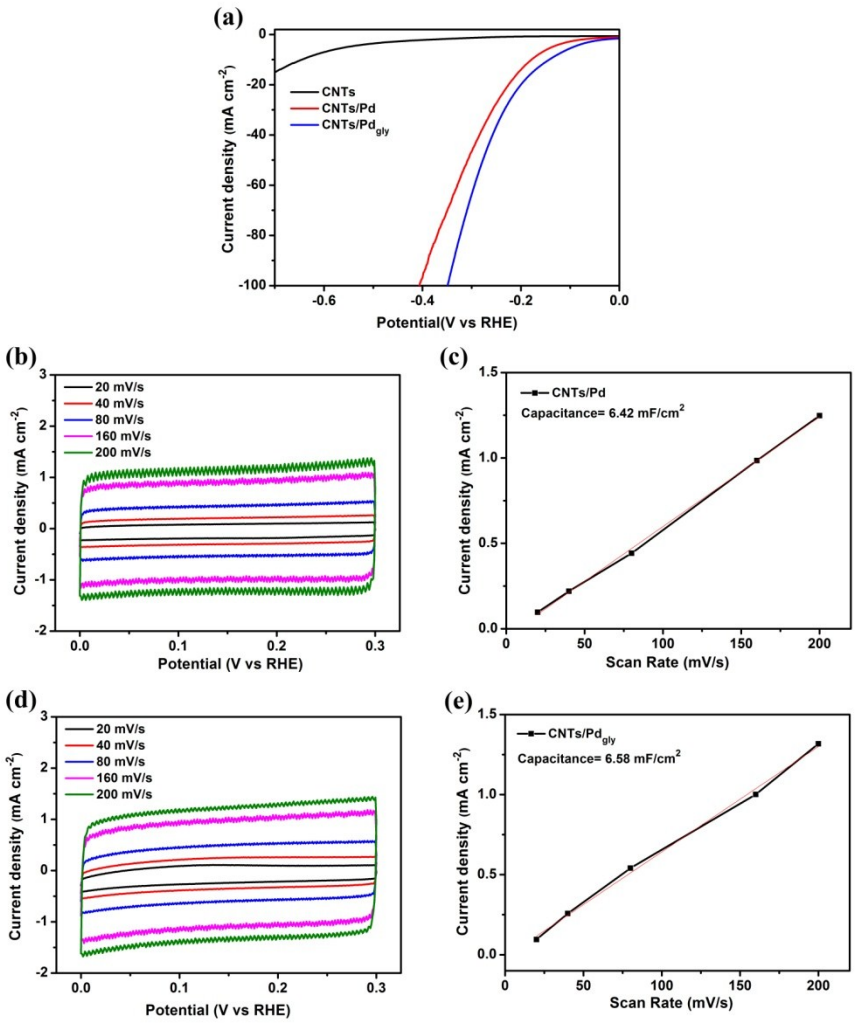

Fig. S23 (a) The polarization curves for CNTs, CNTs/Pd_{gly} and CNTs/Pd in a 0.5 M H_2SO_4 solution at a scan rate of 5 mV s^{-1}. (b-c) The standard CV curves with different scan rates and C_{dl} of CNTs/Pd. (d-e) The standard CV curves with different scan rates and C_{dl} of CNTs/Pd_{gly}.

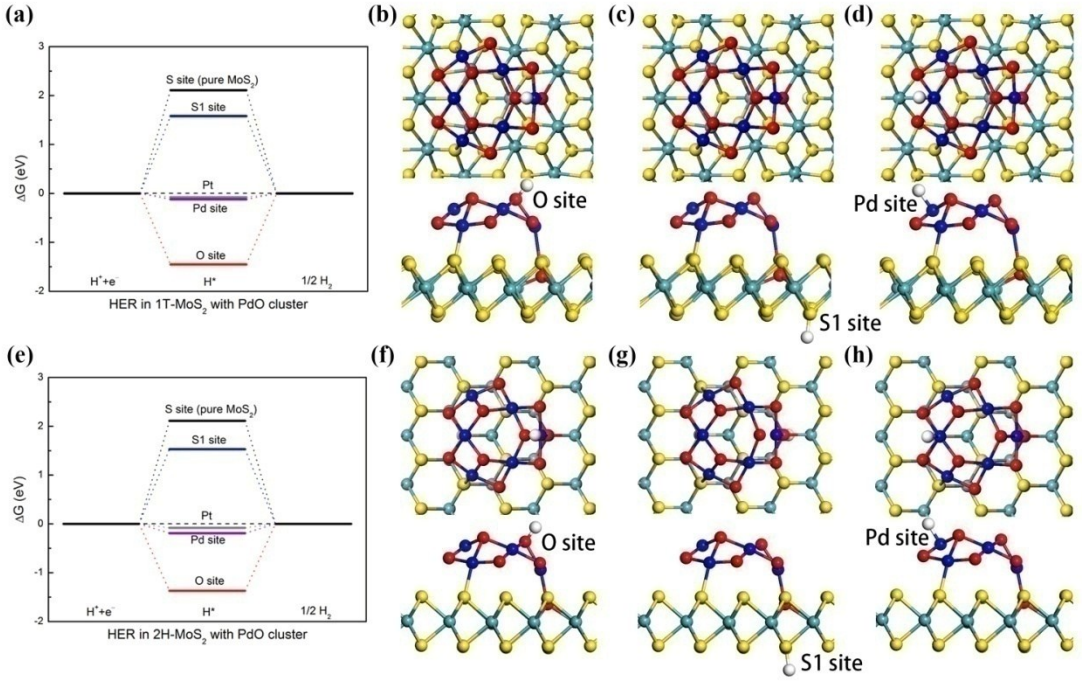

Fig. S24 Binding configurations for single H atom at different adsorbed sites around the PdO clusters located on 1T-MoS_2 and 2H-MoS_2 basal plane, and the Gibbs free energies diagram were given. The blue, olivine, yellow white and red balls were Pd, Mo, S, H and O atoms, respectively.

Table S2. The contents of C, Mo, S, O, N and Pd (in at%) in the different samples.

	C (at%)	Mo (at%)	S (at%)	O (at%)	N (at%)	Pd (at%)
Sub-MoS_x/CNTs	77.13	5.83	14.39	2.65	0	0
Sub-MoS_x/CNTs/Pd_{gly}	76.10	5.12	13.45	4.16	0.54	0.63
Sub-MoS_x/CNTs/Pd	76.55	5.31	13.72	3.67	0	0.75
i-t/MoS_x/CNTs	76.69	6.21	15.03	2.07	0	0
i-t/MoS_x/CNTs/Pd_{gly}	74.51	5.69	14.53	3.95	0.61	0.71
i-t/MoS_x/CNTs/Pd	75.32	5.87	14.70	3.82	0	0.92

Table S3. The contents of Pd and Mo (μg/cm^2) in the different samples

	Pd (μg/cm^2)	Mo (μg/cm^2)
Sub-MoS_x/CNTs/Pd_{gly}	2.8	23.1
i-t/MoS_x/CNTs/Pd_{gly}	3.2	25.6
i-t/MoS_x/CNTs/Pd	4.1	26.5

Table S4. Comparision of HER performance of different samples at a specific overpotential.

	A/mg Pd or Pt	Ref.
Sub-MoS_x/CNTs/Pd_{gly} (at –50 mV)	13.8	Our work
Pt/C (at –50 mV)	0.35	/
Pd^0/GDY (at –50 mV)	7.49	10
Pt-G nanocomposites (at –200 mV)	8.45	11
Pt1/NPC (at –25 mV)	2.86	12
$Pt_1Cu_{1.03}$-D (at –200 mV)	19.34	13

Table S5. Comparision of HER performance in acid media for our electrodeposition sample with other reported electrocatalysts.

Catalyst (pd loading)	Current density (mA cm^{-2})	η at corresponding j(mV vs RHE)	Tafel slope (mV per dec)	Stability	Ref.
C/N-co-doped Ag@Pd NWs	10	111	64	1000 cycles	14
Co@Pd NC	10	175	55.7	10 h	15
$MoSe_2$/Pd	10	231	69	12 h	16
PdNP@N-CNTs	32	100	33	10000 s	17
Pd@PtCu/C	10	19	26.2	10000 cycles	18
Pd-doped WS_2 NF	10	175	54	1000 cycles	19
Pd-SiNW (19.8wt%)	10	153	70	2000 cycles	20
Pd@TNT	10	38	13	25 h	21
Pd-CNx (0.043mgcm^{-2})	10	55	35	48 h	22
PdMnCo alloy (0.285 mg cm^{-2})	10	39	31	80 h	23
Pt@Pd (0.281 mg cm^{-2})	10	56	39	10000 s	24
PtPd bimetallic	10	57	36	10000 s	25
PdCo@CN (0.285 mg cm^{-2})	10	80	31	10000 cycles	26
Sub-MoS_x/CNTs/Pd_{gly}	**10**	**23**	**18**	**24 h**	**Our work**
Pd nanocubes	10	51	62	1000 cycles	27
PdCu@Pd NCs (0.14 mg cm^{-2})	10	31	35	5000 cycles	28
Ni@Pd/PEI–rGO	0.1	59	54	1000 cycles	29
$Pd_{3.02}Te$ NWs/rGO	10	48	63	48h	30
$PdCu_3$ (0.28 mg cm^{-2})	10	50	34	5000 cycles	31

$PdBi_2$ (0.28 mg cm^{-2})	10	78	63	10000 cycles	32
PdPS	10	100	46	1000 cycles	33
Pd_4Se	10	94	50	/	34
$Pd_{17}Se_{15}$	10	182	57	/	34
Pd_7Se_4	10	162	56	/	34

References:

1 D. Wu, Y. Wei, X. Ren, X. Ji, Y. Liu, X. Guo, Z. Liu, A. M. Asiri, Q. Wei, X. Sun, *Adv. Mater.* 2018, **30**, 1705366.

2 T. Wang, J. Zhuo, K. Du, B. Chen, Z. Zhu, Y. Shao and M. Li, *Adv. Mater.*, 2014, **26**, 1400265.

3 Y. Wang, Y. Zhang, S. Zhao, Z. Huang, W. Chen, Y. Zhou, X. Lv and S. Yuan, *Appl. Catal. B- Environ*., 2019, **248**, 44-53.

4 X.-L. Liang, X. Dong, G.-D. Lin and H.-B. Zhang, *Appl. Catal. B-Environ.*, 2009, **88**, 315-322.

5 D. Gao, C. Zhang, S. Wang, Z. Yuan and S. Wang, *Catal. Commun.*, 2008, **9**, 2583-2587.

6 M. Moroseac, T. Skála, K. Veltruská, V. Matolín and I. Matolínová, *Surf. Sci*., 2004, **566**, 1118-1123.

7 J. Yang, Z.Yang, L. Li, Q. Cai, H. Nie, M. Ge, X. Chen , Y. Chen and S. Huang, *Nanoscale*, 2017, **9**, 6886-6894.

8 P. Li, Z. Yang, J. Shen, H. Nie, Q. Cai, L. Li, M. Ge, C. Gu, X. Chen, K. Yang, L. Zhang, Y. Chen and S. Huang, *ACS. Appl. Mater. Interfaces.*, 2016, **8**, 3543-3550.

9 Y.-Y. Liu, H.-P. Zhang, B. Zhu, H.-W. Zhang, L.-D. Fan, X.-Y. Chai, Q.-L. Zhang, J.-H. Liu and C.-X. He, *Electrochim. Acta*, 2018, **283**, 221-227.

10 H. Yu, Y. Xue, B. Huang, L. Hui, C. Zhang, Y. Fang, Y. Liu, Y. Zhao, Y. Li, H. Liu and Y. Li, *iScience*, 2019, **11**, 31-41.

11 F. Liao, W. Shen, Y. Sun, Y. Li, H. Shi and M. Shao, *ACS Sustain. Chem. Eng.*, 2018, **6**, 15238-15244.

12 T. Li, J. Liu, Y. Song and F. Wang, *ACS Catal*. 2018, **8**, 8450-8458.

13 Y. Du, K.Ni, Q. Zhai, Y. Yun, Y. Xu, H. Sheng, Y.Zhu and M. Zhu, *Appl.Catal. A-Gen*. 2018, **557**, 72–78.

14 Y.-Y. Liu, H.-P. Zhang, B. Zhu, H.-W. Zhang, L.-D. Fan, X.-Y. Chai, Q.-L. Zhang, J.-H. Liu and C.-X. He, *Electrochim. Acta*, 2018, **283**, 221-227.

15 H. Yang, Z. Tang, K. Wang, W. Wu, Y. Chen, Z. Ding, Z. Liu and S. Chen, *J. colloid interf. sci.*, 2018, **528**, 18-26.

16 M. D. Sharma, C. Mahala and M. Basu, *J. colloid interf. sci.,* 2019, **534**, 131-141.

17 S. Zhou, X. Chen, P. Yu, F. Gao and L. Mao, *Electrochem. Commun.*, 2018, **90**, 91-95.

18 S. Sarkar and S. C. Peter, *Inorg. Chem.Front.*, 2018, **5**, 2060-2080.

19 A. Hasani, T. P. Nguyen, M. Tekalgne, Q. Van Le, K. S. Choi, T. H. Lee, T. Jung Park, H. W. Jang and S. Y. Kim, *Appl.Catal. A- Gen.*, 2018, **567**, 73-79.

20 K. Yin, Y. Cheng, B. Jiang, F. Liao and M. Shao, *J. colloid interf. Sci.*, 2018, **522**, 242-248.

21 U. Lačnjevac, R. Vasilić, T. Tokarski, G. Cios, P. Żabiński, N. Elezović and N. Krstajić, *Nano Energy*, 2018, **47**, 527-538.

22 T. Bhowmik, M. K. Kundu and S. Barman, *ACS Catal.*, 2016, **6**, 1929-1941.

23 R. Zhang, Z. Sun, R. Feng, Z. Lin, H. Liu, M. Li, Y. Yang, R. Shi, W. Zhang and Q. Chen, *ACS. Appl. Mater. Interfaces*, 2017, **9**, 38419-38427.

24 X.-X. Lin, A.-J. Wang, K.-M. Fang, J. Yuan and J.-J. Feng, *ACS Sustain. Chem.& Eng.*, 2017, **5**, 8675-8683.
25 Z.-Z. Yang, X.-X. Lin, X.-F. Zhang, A.-J. Wang, X.-Y. Zhu and J.-J. Feng, *J. Alloy. Comp.*, 2018, **735**, 2123-2132.
26 J. Chen, G. Xia, P. Jiang, Y. Yang, R. Li, R. Shi, J. Su and Q. Chen, *ACS Appl Mater Interfaces*, 2016, **8**, 13378-13383.
27 J. Li, P. Zhou, F. Li, J. Ma, Y. Liu, X. Zhang, H. Huo, J. Jin and J. Ma, *J.Power Sources*, 2016, **302**, 343-351.
28 J. Li, F. Li, S. X. Guo, J. Zhang and J. Ma, *ACS. Appl. Mater. Interfaces*, 2017, **9**, 8151-8160.
29 J. Li, P. Zhou, F. Li, R. Ren, Y. Liu, J. Niu, J. Ma, X. Zhang, M. Tian, J. Jin and J. Ma, *J. Mater. Chem. A*, 2015, **3**, 11261-11268.
30 L. Jiao, F. Li, X. Li, R. Ren, J. Li, X. Zhou, J. Jin and R. Li, *Nanoscale*, 2015, **7**, 18441-18445.
31 M. Bao, I. S. Amiinu, T. Peng, W. Li, S. Liu, Z. Wang, Z. Pu, D. He, Y. Xiong and S. Mu, *ACS Energy Lett.*, 2018, **3**, 940-945.
32 S. Sarkar, U. Subbarao and S. C. Peter, *J. Mater. Chem. A*, 2017, **5**, 15950-15960.
33 S. Sarkar and S. Sampath, *Chem. Commun.*, 2014, **50**, 7359-7362.
34 S. Kukunuri, P. M. Austeria and S. Sampath, *Chem. Commun.*, 2016, **52**, 206-209.